Nano Futures

PAPER

Ferroelectric phase transitions in multi-domain $K_{0.9}Na_{0.1}NbO_3$ epitaxial thin films

NANO FUTURES

PAPER

Ferroelectric phase transitions in multi-domain $K_{0.9}Na_{0.1}NbO_3$ epitaxial thin films

Laura Bogula[1], Leonard von Helden[1], Carsten Richter[1], Michael Hanke[2], Jutta Schwarzkopf[1] and Martin Schmidbauer[1]

[1] Leibniz-Institut für Kristallzüchtung, 12489, Berlin, Germany
[2] Paul-Drude Institut für Festkörperelektronik, 10117, Berlin, Germany

E-mail: laura.bogula@ikz-berlin.de

RECEIVED
12 June 2020

ACCEPTED FOR PUBLICATION
22 June 2020

PUBLISHED
3 August 2020

Keywords: ferroelectric domains, epitaxial strain, lead-free piezoelectric thin films, (K, Na)NbO_3, phase transition, x-ray diffraction

Abstract

A high-temperature phase transition in strained ferroelectric $K_{0.9}Na_{0.1}NbO_3$ thin films epitaxially grown on orthorhombic (110) $NdScO_3$ substrates is identified and investigated by *in situ* x-ray diffraction and piezoresponse force microscopy. At room temperature, the thin films exhibit a highly anisotropic misfit strain, inducing the occurrence of monoclinic a_1a_2/M_C phases and manifesting itself in the formation of a highly regular, herringbone-like domain arrangement. With increasing temperature, a ferroelectric-to-ferroelectric phase transition to an orthorhombic a_1/a_2 phase with exclusive lateral electrical polarization takes place. Within a wide temperature range from 180 °C to about 260 °C, a coexistence of the monoclinic a_1a_2/M_C room temperature phases and the orthorhombic a_1/a_2 high temperature phase is observed. Finally, at higher temperatures only the orthorhombic a_1/a_2 phase, which is arranged in a regular stripe domain pattern, is present. Corresponding simulations of the scattered x-ray intensity patterns show that the orthorhombic unit cells undergo a small in-plane rotation. This leads to four different in-plane orientations of the orthorhombic unit cells and four corresponding variants of superdomains.

1. Introduction

Piezo- and ferroelectric materials are of great interest for a variety of technological applications, ranging from ferroelectric capacitors made from bulk material to memory and sensor devices [1, 2], where also thin films are required [3]. Besides the possibility of using thin films for miniaturizing piezoelectric devices, it is even more important to note that the inherent piezoelectric properties can be modified by the application of epitaxial strain. Strain engineering can either offer the possibility to intentionally tune the ferro-/piezoelectric properties [4] or lead to the formation of new ferroelectric phases with crystallographic symmetries that are not stable in unstrained bulk crystals [5–7]. In particular, monoclinic ferroelectric phases have been in the focus of recent research since they offer strongly enhanced piezoelectric coefficients [8–10].

In recent years, the lead-free solid solution $K_xNa_{1-x}NbO_3$ has gained increasing attention, as a very promising candidate to replace hazardous $PbZr_xTi_{1-x}O_3$ that is still widely used due to its excellent piezoelectric properties [11]. $K_xNa_{1-x}NbO_3$ exhibits promising piezoelectric properties already in its bulk form [12, 13]. Furthermore, strained thin films made of $K_xNa_{1-x}NbO_3$ are of particular interest, since a variety of different monoclinic ferroelectric phases have been theoretically predicted [14–16] and experimentally confirmed [17–19]. Practically, the epitaxial strain can be tuned by changing the film stoichiometry (potassium molar concentration x) and the substrate material. Moreover, many material properties of a ferroelectric material improve drastically at or in the proximity of phase transitions. This is reflected, for example, in significantly increased piezoelectric constants as calculated in [20] for bulk $KNbO_3$. In order to exploit this for technological applications, a detailed knowledge of the phase stabilities and phase transitions is essential.

In a previous paper it was demonstrated, that the choice of suitable strain conditions leads to a coexistence of two different monoclinic phases at room temperature: $K_{0.9}Na_{0.1}NbO_3$ thin films grown on

orthorhombic (110) $NdScO_3$ exhibit a characteristic anisotropic misfit strain, leading to the simultaneous existence of in-plane a_1a_2 monoclinic phase and inclined M_C monoclinic phase [21]. The delicate balance between these monoclinic phases induces a complex but regular herringbone-like domain pattern with alternating a_1a_2/M_C domain arrangement. Phase transitions in these multi-domain thin films are of particular interest, since the different ferroelectric phases can inherently undergo different phase transitions. Owing to their complex electrical and elastic boundary conditions, they potentially provide a higher degree of freedom during the transition since e.g. volume ratios of different domain types can be changed.

In this paper we identify and discuss a high temperature ferroelectric-to-ferroelectric phase transition in $K_{0.9}Na_{0.1}NbO_3$/(110) $NdScO_3$ thin films. We demonstrate that during the phase transition the room temperature a_1a_2/M_C herringbone domain pattern is converted into a regular orthorhombic a_1/a_2 stripe domain pattern. It is particularly noteworthy that the observed phase transition is not abrupt but extends over a wide temperature range from 180 °C to about 260 °C within which monoclinic and orthorhombic phases coexist. This surprising behavior is probably a consequence of the complicated stability conditions that prevail in the presence of coexisting ferroelectric phases.

2. Experimental

$K_{0.9}Na_{0.1}NbO_3$ thin films were epitaxially grown on (110) $NdScO_3$ orthorhombic substrates by liquid-delivery spin metalorganic vapor phase epitaxy. With this technique, growth takes place close to the thermodynamic equilibrium and at comparatively high oxygen partial pressures of typically 10–20 mbar. This leads to nearly perfect, quasi-defect-free thin films with smooth surfaces and interfaces as well as very regular ferroelectric domain patterns. More details about the growth parameters can be found in [19] and [22]. In order to visualize the ferroelectric domain pattern of the epitaxial layers piezoresponse force microscopy (Asylum Research, MFP-3D standalone) was employed in dual AC resonance tracking mode. A heating stage allows measurements in air up to 300 °C.

X-ray diffraction techniques are particularly suitable for the investigation of phase transitions, as both, changes in the crystal symmetry and corresponding modifications in the periodic arrangement of ferroelectric domains, can be easily identified. For the $K_{0.9}Na_{0.1}NbO_3$ epitaxial layers, grazing incidence in-plane x-ray diffraction (GIXD) turned out to be most advantageous. On the one hand, owing to the small penetration depths of just a few tens of nanometers, the scattering signal from the thin epitaxial layer is greatly enhanced as compared to the signal of the underlying substrate. On the other hand, the scattering geometry is particularly sensitive to in-plane lattice distortions.

GIXD measurements have been carried out using synchrotron radiation at P08 station of PETRA III (DESY, Hamburg) and KMC-2 station of BESSY II (Helmholtz-Zentrum Berlin) at a photon energy of 8 keV. For heating, an Anton Paar DHS 1100 temperature chamber was used under ambient conditions (in air). To ensure good thermal contact, samples were glued on a Cu sample holder, which was mounted directly on the heating plate. Using a high-framerate position-sensitive detector the two-dimensional (2D) in-plane intensity distributions can be measured effectively with typical acquisition times of several tens of minutes [23]. In order to disentangle the signal from

(i) the periodic arrangement of the domains, which leads to equidistantly spaced sharp satellite peaks and
(ii) the different symmetry of individual domains, which leads to a characteristic peak splitting depending on the scattering vector $\vec{Q}$

A set of Bragg reflections has to be measured. In the following, we use the notation of crystallographic directions and Bragg reflections corresponding to the orthorhombic (110) $NdScO_3$ substrate (a = 5.577 Å, b = 5.777 Å, c = 8.005 Å [24],). The main pseudocubic axes [25] of the epitaxial $K_{0.9}Na_{0.1}NbO_3$ layers are parallel to the in-plane substrate directions $[\bar{1}10]$ and [001]. More details and visualization can be found in [21].

3. Results and discussion

3.1. Monoclinic room temperature structure

The ferroelectric domain pattern of a strained $K_{0.9}Na_{0.1}NbO_3$ thin film (38 nm) grown epitaxially on a (110) $NdScO_3$ orthorhombic substrate shows a complex herringbone-like domain formation, observed in the lateral piezoresponse [PR = amplitude × sin(phase)] micrograph, as depicted in figure 1(a). A schematic zoom into the domain pattern visualized in figure 1(b) illustrates that the herringbone domain pattern consists of two equivalent but differently oriented phases with monoclinic symmetry and space group Pm, namely a_1a_2 and M_C [21]. For both phases, exemplary unit cells are depicted in figure 1(b) in their

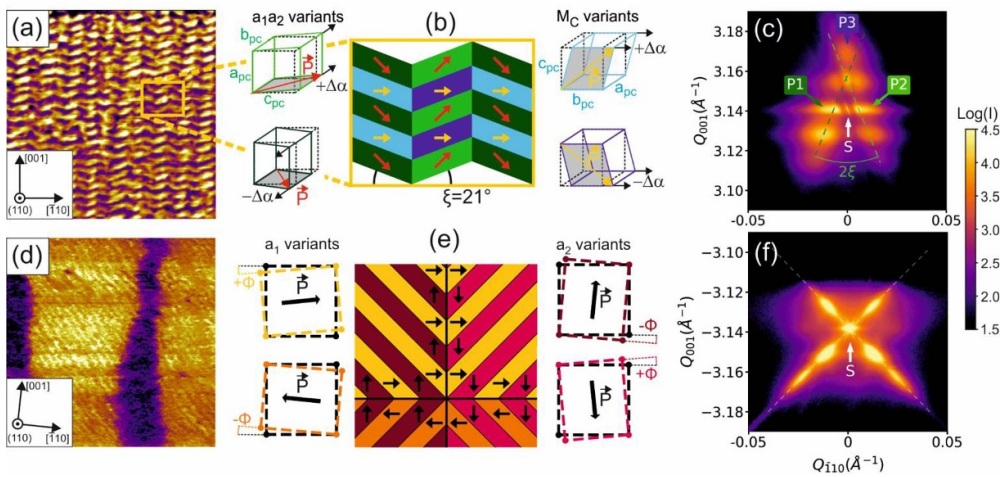

Figure 1. $1 \times 1\ \mu m^2$ lateral piezoresponse force micrographs of a 38 nm $K_{0.9}Na_{0.1}NbO_3$ thin film grown on (110) $NdScO_3$ substrate measured at room temperature (a) and 250 °C (d) along with schematic real space models (b), (e) and corresponding GIXD pattern around the 004 Bragg reflection at room temperature (c) and the equivalent $00\bar{4}$ Bragg reflection at 380 °C (f).

pseudocubic notation with lattice parameters a_{pc}, b_{pc}, c_{pc} and monoclinic shearing angles $\Delta\alpha$ that denote the deviation from the 90° angle. Due to the different orientations of the pseudocubic unit cell on the substrate, the corresponding polarization vectors—which lie within the monoclinically sheared b_{pc}-c_{pc}-plane—also have different directions. Within the a_1a_2 variants—depicted in dark and light green—the monoclinic unit cells have an alternating in-plane monoclinic distortion and corresponding in-plane polarization vectors $\vec{P}$ (red arrows). In contrast, the dark and light blue M_C domains exhibit an out-of-plane monoclinic distortion and thus an inclined polarization vector, with in-plane and out-of-plane components, indicated by yellow arrows. The same color code is used to represent their in-plane polarization components in the schematic top view in figure 1(b). Furthermore, the alternating in-plane angles of the domain walls with respect to the $[\bar{1}10]$ direction ($\xi = \pm 21°$) are marked in figure 1(b). More detailed information about the room temperature domain structure and corresponding monoclinic phases can be found in [21, 26, 27].

The herringbone domain pattern leads to a characteristic x-ray diffraction pattern. Exemplarily, the 2D intensity distribution in the vicinity of the in-plane 004 $NdScO_3$ Bragg reflection is shown in figure 1(c). Apart from the sharp peak S caused by the substrate, information about the domain arrangement as well as the crystal symmetry of both the a_1a_2 and the M_C phases can be obtained. The a_1a_2 domain arrangement, which is characterized by alternating in-plane shearing, leads to the peak splitting P1 and P2, and their distance $\Delta Q_{\bar{1}10}$ is related to the in-plane monoclinic distortion angle $\Delta\alpha$ by $\tan(\Delta\alpha) = \frac{\Delta Q_{\bar{1}10}}{2Q_{001}}$, such that $\Delta\alpha = 0.14°$. Analysis of a number of Bragg reflections has shown that in addition, a peak P3 can be identified, originating from the M_C domains and—in contrast to the a_1a_2 domains—exhibiting no in-plane splitting [26]. Superimposed on these three peaks, pronounced equidistantly spaced satellite peaks arise, which are aligned along the green dotted lines. They are caused by the periodic arrangement of the a_1a_2/M_C domains. From the opening angle of the satellite branches an in-plane domain wall angle of $\xi = \pm 21°$ can be evaluated, which is in good agreement with the PFM image shown in figure 1(a).

3.2. Orthorhombic high temperature structure

At higher temperatures, e.g. at 250 °C, ferroelectric domains are still observed, as shown in the lateral piezoresponse force micrograph in figure 1(d). Yet, when compared to the room temperature micrograph in figure 1(a), a significant change in the ferroelectric domain pattern is apparent, indicating a ferroelectric-to-ferroelectric phase transition. The herringbone-like domain arrangement, present at room temperature, changes into a regular stripe domain pattern, which forms superdomains visible as brighter and darker regions. Within the bright superdomain, small stripes of about 31 nm are periodically aligned along the in-plane diagonal and exhibit exclusive lateral electrical polarization. Such domain patterns are known to be caused by a_1/a_2 domains [28, 29]. Usually, a_1/a_2 unit cells are attributed to tetragonal symmetry, however, as the underlying substrate is orthorhombic with rectangular (non-quadratic) surface unit cells, the a_1/a_2 unit cell symmetry is reduced to orthorhombic symmetry. Consulting group/subgroup relations for monoclinic point group m, the only orthorhombic point group that is directly connected and ferroelectric is mm2 [30]. Starting from monoclinic Pm symmetry with only one single mirror plane as non-trivial symmetry element, a phase transition to orthorhombic Pmm2 is very plausible, as only two symmetry elements have to be added

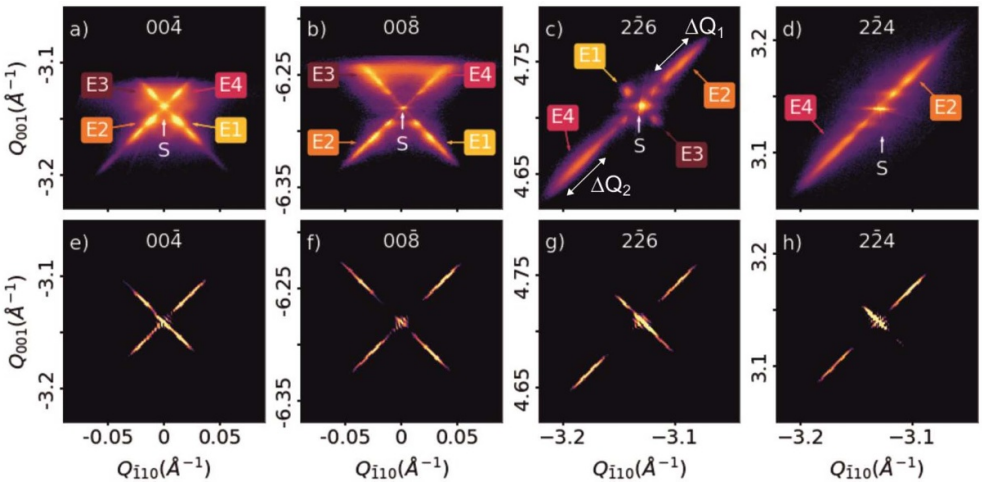

Figure 2. Top row: experimental GIXD patterns for the high temperature phase measured in the vicinity of different $NdScO_3$ Bragg reflections, labeled by S. The experimental intensity patterns were recorded at 380 °C (a), (b), (d) and 300 °C (c), i.e. at temperatures where only the a_1/a_2 phase is present. Bottom row: corresponding simulations.

(a second mirror plane m and a 2-fold rotation axis). Due to the absence of inversion symmetry, Pmm2 is still ferroelectric. Space group Pmm2, has already been denoted for orthorhombic a_1/a_2 domains in [31].

The associated 00$\bar{4}$ GIXD reflection is shown in figure 1(f) for 380 °C. While it looks simpler compared to the room temperature measurement, a number of different scattering features are still visible and need to be disentangled. At first sight, two diagonal branches of sharp, equidistant peaks are visible. Upon comparison with further Bragg reflections (shown in the top row of figure 2), it is found that the distances between the sharp satellite peaks are identical, regardless of the Bragg reflection selected. Therefore, these diagonal satellite peaks are caused by the uniform arrangement of the stripe domains and the evaluated periodicity of about 31 nm is in excellent agreement with the PFM result. Due to the presence of two satellite branches along both in-plane diagonal directions, there have to be stripe domains aligned along both in-plane diagonal directions as shown in the domain model in figure 1(e). Although they cannot be directly detected in the PFM image we suspect that these 90° rotated stripe domains are present within the dark regions in figure 1(d). Another feature of the GIXD pattern appears upon comparison of different Bragg reflections. Four of them are displayed in figure 2 namely 00$\bar{4}$ (a), 00$\bar{8}$ (b), 2$\bar{2}$6 (c) and 2$\bar{2}$4 (d). While the satellite peaks remain at constant distance for all Bragg reflections, there are additional elongated features (called streaks, hereafter) whose position depends on the respective scattering vector $\vec{Q}$. These streaks are labeled by E1-E4. For the 00$\bar{4}$ Bragg reflection in figure 2(a), which has a small length of $\vec{Q}$, they are located close to S and overlap with the strong satellite reflections caused by the domain periodicity. With increasing length of the scattering vector, the streaks E1-E4 disperse outwards as can be clearly observed for the 00$\bar{8}$, 2$\bar{2}$6 and 2$\bar{2}$4 Bragg reflections. Additionally, the streaks are asymmetrically arranged with respect to the central substrate reflection S. This is particularly pronounced in figures 2(c) and (d). The observed Q-dependence of E1-E4 suggests that they are caused by a unit cell deformation.

In order to be able to explain all presented results, a structural model is proposed, which is shown in figure 1(e). Stripe domains with a diagonal periodicity of 31 nm build up larger superdomains, within which the in-plane domain walls are aligned along one of the two in-plane diagonal directions. However, in order to create four different streaks E1-E4, four different variants of the orthorhombic unit cell are required, which are schematically shown in top view in figure 1(e). The unit cell deformation is a combination of an in-plane rotation and a scaling of the in-plane lattice parameters, such that two corners of the orthorhombic unit cells can be kept fixed. This is necessary to explain for example the absence of E1 and E3 in the 2$\bar{2}$4 Bragg reflection in figure 2(d). In general, for Bragg reflections with reciprocal lattice vectors aligned perpendicular to the domain walls (i.e. reflections with Miller indices h$\bar{h}$2h or $\bar{h}$h2h), two of the four streaks coincide with the substrate Bragg reflection. Therefore, the corresponding net-planes must remain unaffected by the unit cell deformation and the associated streaks cannot stem from a simple rotation of the unit cell since this would move all lattice points. The four variants are divided into a_1 cells shown on the left and a_2 cells shown on the right in figure 1(e), depending on the alignment of their long axis. The black arrows in the middle of each unit cell indicate the corresponding electrical polarization vectors, which exhibit exclusive in-plane orientation. Arranging a_1/a_2 stripe domains within larger superdomains, four different types are possible as depicted in the domain model in figure 1(e).

To demonstrate the validity of our structural domain model, it was used to calculate the corresponding x-ray diffraction patterns, which can then be compared with the measurements as shown in figure 2. All above mentioned characteristics of the domain structure of the ferroelectric high temperature phase are reflected in associated features in the scattered intensity distribution. The satellite reflection branches from periodic stripe arrangement can already be reproduced by a two-dimensional fast Fourier transformation of the PFM micrographs, which is, in fact, how the stripe periodicity has been extracted. For the streaks (labeled by E1-E4 in the corresponding figures), however, atomic scale unit cells have to be considered. Therefore, the 2D real space domain pattern is constructed from unit cells j, with x_j and y_j as the corresponding in-plane coordinates along the $[\bar{1}10]$ and [001] substrate directions, respectively. The scattered intensity of the domain pattern is then calculated using kinematic theory of x-ray diffraction [32].

The main objective of the simulations was a correct reproduction of the experimentally observed streaks E1-E4 shown in figure 2 (top), while the periodic arrangement of the domains plays a subordinate role. For that reason, a simplified domain arrangement has been used with only one stripe domain per unit cell variant. Comparing the simulations of the streaks to the corresponding experimental results in figure 2, a very good agreement can be observed, confirming the validity of our real space model. Due to the combination of scaling and rotation of the unit cells, simulations are necessary to extract the in-plane lattice parameters and rotation angles. They cannot be calculated as easily as, e.g. the monoclinic distortion angle $\Delta\alpha$ of the a_1a_2 domains in the room temperature structure that follows directly from the P1/P2 distance.

Another feature included in the domain model and the calculations is the characteristic asymmetry in the streaks E1-E4, which manifests itself in different peak widths and different peak positions relative to the central substrate reflection S. This asymmetry is particularly pronounced for the $2\bar{2}6$ Bragg reflection (figure 2(c)). The different peak widths ΔQ_1 and ΔQ_2 are related to different lateral widths w_1 and w_2 of the a_1 and a_2 domains, respectively. For rectangular domains we can use the expression $w_j = 2\pi/\Delta Q_j$ (j = 1,2) and have evaluated values of $w_1 = 17.2$ nm and $w_2 = 14.7$ nm. The corresponding sum $w_1 + w_2 = 31.9$ nm is in excellent agreement with the observed periodicity of 31 nm, which is derived from the peak spacing in the x-ray diffraction satellite pattern and the PFM micrograph. Unfortunately, at 250 °C the resolution of the PFM micrograph is not high enough to confirm different lateral widths in the individual a_1 and a_2 stripe domains directly in real-space. In addition to the different peak widths, a pronounced asymmetry of the positions of E1/E2 (a_1 domains) and E3/E4 (a_2 domains) relative to the central substrate reflection S is observed in all investigated Bragg reflections (figure 2 top). To take this asymmetry into account, different rotation angles were used in the simulations for the a_1 and a_2 domains. The best agreement between experiment and simulation is achieved with $\phi = \pm 0.25°$ for the a_1 domains and with $\phi = \pm 0.35°$ for the a_2 domains. The observation that the wider a_1 domains exhibit a smaller rotation angle, while the narrow a_2 domains show a larger rotation angle is consistent with the concept of minimizing the total free energy, which is usually considered to drive domain formation [33]. Due to the substrate to which the thin film is pinned, a rigid in-plane rotation of unit cells within one large domain requires a greater elastic energy density than within a small domain. To understand the mechanisms behind the unit cell deformations, further work is necessary.

3.3. Phase transition regime

In order to analyze the phase transition itself, the scattered intensity distribution in the vicinity of the in-plane $2\bar{2}4$ substrate Bragg reflection (labeled by S) is investigated in temperature steps of 40 °C. At room temperature the GIXD patterns of the 004 and $2\bar{2}4$ Bragg reflections look very similar. Again, the peaks P1/P2 from the a_1a_2 domains along with their respective satellite branches and the peak P3 from the M_C domains can be identified as shown in figure 3(a). On first sight, upon heating up to 140 °C (figure 3(b)), the diffraction pattern looks identical to the room temperature intensity distribution. However, the intensity of the peaks P1, P2 and P3 associated with the herringbone domain pattern decreases, while at the same time increased diffuse scattering appears. At 180 °C (figure 3(c)) the scattered intensity from the herringbone domains is so small, that the weak peak P3 is no longer observed, while the more intense peaks P1/P2 are still visible. Also the herringbone domain angle remains at the room temperature value of $\xi = \pm 21°$. The originally unstructured diffuse intensity cloud is now aligned along the in-plane diagonal direction as indicated by the white dotted line. A further increase of the temperature to 220 °C (figure 3(d)) leads to the appearance of equidistant satellite peaks, proving that the regular stripe pattern of the a_1/a_2 domains has formed, while P1 and P2 still persist. With further temperature increase to 260 °C (figure 3(e)) the already discussed streaks appear (designated as E2 and E4), which are elongated along the in-plane diagonal. At this point the phase transition is completed and a further increase in temperature does not change the overall appearance of the intensity distribution. However, with increasing temperature, the relative distance between the streaks E2 and E4 decreases as can be seen for the measurement at 420 °C in figure 3(f). At the same time, they become weaker until they can no longer be observed at 460 °C (figure 3(g)). Additionally, the intensity

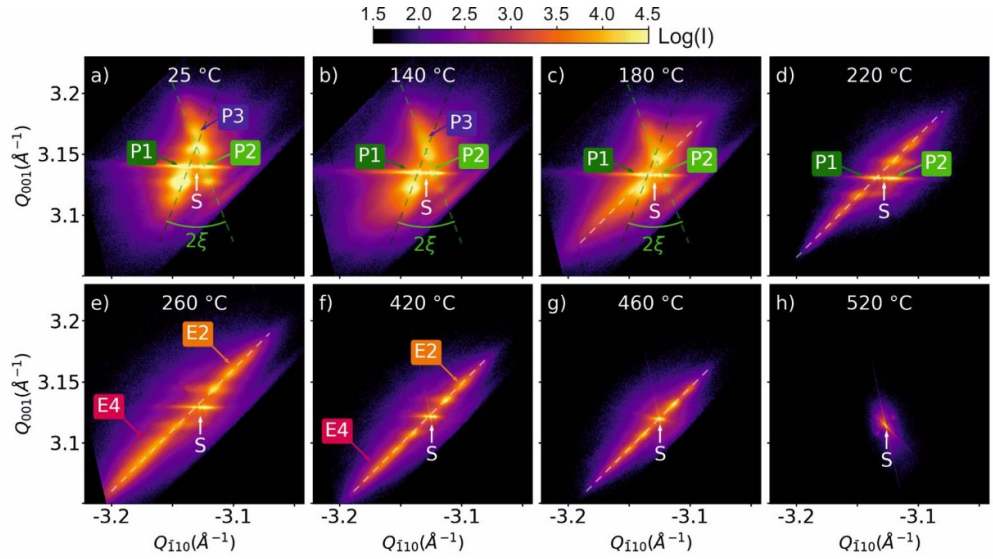

Figure 3. In-plane GIXD patterns around the $2\bar{2}4$ $NdScO_3$ Bragg reflection (labeled with S) with increasing temperature in the range of 25 °C to 520 °C. A gradual phase transition from the herringbone-like domain pattern (a) and (b) to the high temperature pattern (e) and (f) occurs with a broad coexistence regime (c) and (d). At 460 °C the absence of the streaks E2 and E4 indicates the beginning of a second phase transition to the paraelectric phase which is reached at about 520 °C (h).

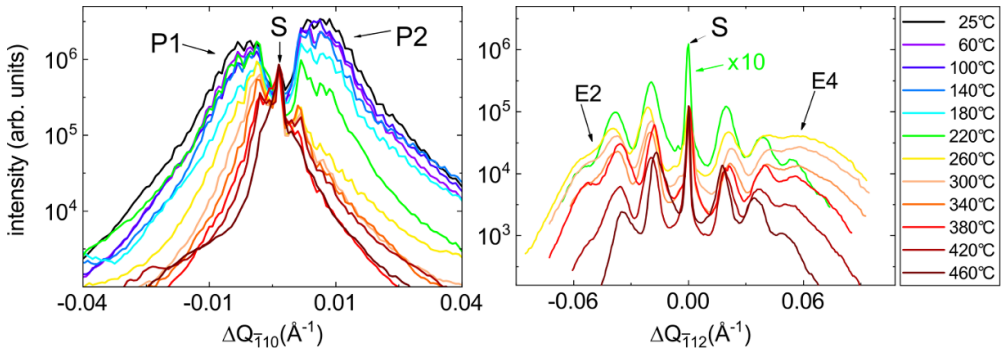

Figure 4. Intensity profiles as a function of temperature taken from $2\bar{2}4$ GIXD reflections (compare figure 3) along (a) $Q_{\bar{1}10}$ and (b) $Q_{\bar{1}12}$. The intensities have been normalized to the central substrate Bragg reflection S.

of the satellite peaks reduces until at about 520 °C (figure 3(h)) a second phase transition is found, where no satellite peaks are observed, indicating the absence of a periodic domain pattern. This result corresponds to the expectation to reach the paraelectric phase at these higher temperatures.

In order to analyze the changes of the diffraction pattern as a function of temperature in more detail, horizontal line profiles containing the substrate reflection S and diagonal line profiles along the white dashed lines in figure 3 are shown in figures 4(a) and (b), respectively. The horizontal line profile is used to monitor the intensities of P1 and P2 and their mutual splitting. At room temperature the features P1/P2 are very broad and also show a two/four times higher intensity than the substrate peak S. The width of P1/P2 is correlated to the individual domain size along the $[\bar{1}10]$ direction and can be estimated as 150 nm, which is in good agreement with the PFM results (140 nm, see also figure 1(a)). While the widths of P1 and P2 remain approximately constant, their relative splitting and thus the in-plane monoclinic angle slightly decreases upon increasing temperatures. Additionally, their intensity decreases, which is a strong indication that the volume fraction of a_1a_2 domains in the thin film is reducing. With a further rise in temperature up to 260 °C we observe a dramatic change in the appearance of the peaks, which manifests itself in a pronounced sharpening and a strong shift of $\Delta Q_{\bar{1}10}$ towards zero. We conclude that at a temperature of 260 °C no a_1a_2 domains are present in the layer anymore. Instead, the sharp peaks are presumably generated by well-ordered superdomains of the new high temperature phase. Finally, these sharp peaks disappear at 460 °C, indicating the beginning of the next phase transition, which is reached at about 520 °C, where the film does not show any periodic domain pattern.

For temperatures above 220 °C, diagonal line profiles are of particular interest, as shown in figure 4(b). All curves feature equidistant satellite reflections around the substrate reflection S. However, comparing the curves for 220 °C and 260 °C, the appearance of additional features E2 and E4 at 260 °C becomes clear. For higher temperatures, their positions shift slightly inwards and their intensity decrease until at 460 °C only the sharp, equidistant satellite reflections are visible. At this temperature supposedly 'normal', i.e. unrotated a_1/a_2 domains are present. Here, the different polarization vector directions in the respective a_1 and a_2 domains still lead to sufficient contrast in the GIXD measurements. Therefore, a satellite diffraction pattern can still be observed.

Our study shows that a ferroelectric-to-ferroelectric phase transition takes place in the broad temperature range from 180 °C to about 260 °C in which the ferroelectric room temperature and ferroelectric high temperature phases coexist. A coexistence of phases with different symmetries has also been observed in bulk piezoelectrics near the morphotropic phase boundary and has been shown to enhance the piezoelectric properties of the material [34, 35]. The increased number of possible polarization orientations [34] and the flat energy profile enable polarization rotation [36], which is the widely accepted mechanism behind ultrahigh eletromechanical response at the morphotropic phase boundaries [37].

On the basis of our experimental data, however, we cannot decide whether there is an interaction of the different ferroelectric phases within the coexisting regime, or whether they exist in well separated macroscopic areas. Nonetheless, the ferroelectric room temperature phase (i.e. the herringbone pattern) already shows a tailored architecture in which an intended coexistence of two ferroelectric monoclinic phases (in-plane a_1a_2 and inclined M_C phase) has been created. The phase transition we observed now adds a third ferroelectric phase with pure horizontal polarization. To what extent this has a positive effect on the piezoelectric properties is not clear yet.

Compared to less complex ferroelectric domain patterns, consisting of only a single monoclinic phase, the observation of such a broad phase transition regime is a major qualitative difference. For example, in compressively strained $K_xNa_{1-x}NbO_3$ thin films showing M_C stripe domains, a ferroelectric-to-ferroelectric phase transition from the monoclinic M_C into an orthorhombic c phase has been found [38]. Despite the huge shift in phase transition temperature depending on the misfit strain, no extended temperature range was observed in which both monoclinic and orthorhombic phases coexist. Exemplarily, for $K_{0.7}Na_{0.3}NbO_3$ thin films grown on (110) $TbScO_3$, the phase transition occurrs at T = 115 °C sharp. Presumably, the complex domain arrangement in a herringbone-like domain pattern shows a higher degree of freedom in adapting the boundary conditions such as lattice strains and electrostatic fields, which leads to a coexistence of different symmetries in the phase transition regime.

3. Conclusions

The characteristic room temperature herringbone domain pattern, consisting of ferroelectric monoclinic a_1a_2/M_C domains, transforms into a periodic ferroelectric a_1/a_2 stripe domain pattern with orthorhombic symmetry. Interestingly, the orthorhombic cells do not exactly follow the in-plane symmetry of the underlying substrate but undergo a small in-plane distortion, resulting in the formation of four different unit cell and domain variants. Most remarkably, we find an unusually wide temperature regime between 180 °C and about 260 °C in which the phase transition to the orthorhombic a_1/a_2 phase takes place and in which both room temperature and high temperature phases coexist. The effect of the broad phase transition region on the piezoelectric properties, however, needs further investigation.

Acknowledgments

We thank DESY Hamburg and Helmholtz-Zentrum Berlin for providing beam time at P08 (proposal I-20170645) and KMC-2 station (proposal 182-07317-ST), respectively. In particular we are grateful to Florian Bertram and Daniel Többens for assistance with the x-ray diffraction experiments and to Michaela Klann for sample growth. The $NdScO_3$ substrates were grown at Leibniz-Institut für Kristallzüchtung (group of Steffen Ganschow). We thank EFRE (Project number 1.8/15) and DFG (Project number FE 1438/2-1) for the funding of this project. Finally, we appreciate fruitful discussions with Jos Boschker and Peter Gaal.

ORCID iDs

Laura Bogula https://orcid.org/0000-0003-1308-4242
Leonard von Helden https://orcid.org/0000-0001-8052-1444
Carsten Richter https://orcid.org/0000-0002-4230-215X
Jutta Schwarzkopf https://orcid.org/0000-0002-8919-3608

Martin Schmidbauer https://orcid.org/0000-0003-1014-7332

References

[1] Haertling G H 2007 *Ferroelectr. Fundam. Collect.* **818** 157–78
[2] Setter N *et al* 2006 *J. Phys. D: Appl. Phys.* **100** 0–46
[3] Martin L W and Rappe A M 2016 *Nat. Rev. Mater.* **2** 16087
[4] Zeches R J *et al* 2009 *Science* **326** 977–80
[5] Pertsev N A, Zembilgotov A G and Tagantsev A K 1998 Phys. *Rev. Lett.* **80** 1988–91
[6] Koukhar V G, Pertsev N A and Waser R 2001 *Phys. Rev.* B **64** 1–15
[7] Sheng G, Zhang J X, Li Y L, Choudhury S, Jia Q X, Liu Z K and Chen L Q 2008 Appl. *Phys. Lett.* **93** 2008–10
[8] Everhardt A S, Matzen S, Domingo N, Catalan G and Noheda B 2016 *Adv. Electron. Mater.* **2** 1500214
[9] Guo R, Cross L E, Park S E, Noheda B, Cox D E and Shirane G 2000 *Phys. Rev. Lett.* **84** 5423–6
[10] Chen Z *et al* 2011 *Adv. Funct. Mater.* **21** 133–8
[11] Zhang S, Li F, Yu F, Jiang X, Lee H Y, Luo J and Shrout T R 2018 *J. Korean Ceram. Soc.* **55** 419–39
[12] Hu C *et al* 2020 *Sci. Adv.* **6** eaay5979
[13] Koruza J, Liu H, Höfling M, Zhang M H and Veber P 2020 *J. Mater. Res.* **35** 1–27
[14] Bai G and Ma W 2010 *Physica* B **405** 1901–7
[15] Zhou M-J, Wang -J-J, Chen L-Q and Nan C-W 2018 *J. Phys. D: Appl. Phys.* **123** 154106–1
[16] Wang B, Chen H-N, Wang -J-J and Chen L-Q 2019 *Appl. Phys. Lett.* **115** 092902
[17] Luo J, Sun W, Zhou Z, Lee H Y, Wang K, Zhu F, Bai Y, Wang Z J and Li J F 2017 *Adv. Electron. Mater.* **3** 1–8
[18] Luo J *et al* 2017 *ACS Appl. Mater. Interfaces* **9** 13315–22
[19] Schwarzkopf J, Braun D, Hanke M, Uecker R and Schmidbauer M 2017 *Frontiers Mater.* **4** 26
[20] Liang L, Li Y L, Hu S Y, Chen L Q and Lu G H 2010 *J. Phys. D: Appl. Phys.* **108** 094111
[21] Schmidbauer M, Braun D, Markurt T, Hanke M and Schwarzkopf J 2017 *Nanotechnology* **28** 24LT02
[22] Schwarzkopf J, Schmidbauer M, Remmele T, Duk A, Kwasniewski A, Bin Anooz S, Devi A and Fornari R 2012 *J. Appl. Crystallogr.* **45** 1015–23
[23] Schmidbauer M, Schäfer P, Besedin S, Grigoriev D, Köhler R and Hanke M 2008 *J. Synchrotron Radiat.* **15** 549–57
[24] Veličkov B, Kahlenberg V, Bertram R and Bernhagen M 2007 *Z. Kristallogr.* **222** 466–73
[25] Vailionis A, Boschker H, Siemons W, Houwman E P, Blank D H A, Rijnders G and Koster G 2011 *Phys. Rev.* B **83** 1–10
[26] Braun D, Schmidbauer M, Hanke M and Schwarzkopf J 2018 *Nanotechnology* **29** 015701
[27] Braun D, Schmidbauer M, Hanke M, Kwasniewski A and Schwarzkopf J 2017 *Appl. Phys. Lett.* **110** 232903
[28] Pompe W, Gong X, Suo Z and Speck J S 1993 *J. Phys. D: Appl. Phys.* **74** 6012–9
[29] Alpay S P and Roytburd A L 1998 *J. Phys. D: Appl. Phys.* **83** 4714–23
[30] *International tables for crystallography volume A: space-group symmetry* (https://doi.org/10.1107/97809553602060000114)
[31] Janolin P E 2009 *J. Mater. Sci.* **44** 5025–48
[32] Als-Nielsen J and McMorrow D 2011 *Elements of Modern X-ray Physics* (New York: Wiley)
[33] Fesenko E G, Gavrilyatchenko V G and Semenchev A F 1989 *Ferroelectrics* **100** 195–207
[34] Yang Y, Zhou Y, Ren J, Zheng Q, Lam K H and Lin D 2018 *J. Eur. Ceram. Soc.* **38** 557–66
[35] Lu X, Zhang H, Zheng L and Cao W 2016 *AIP Adv.* **6** 105208
[36] Damjanovic D 2010 *Appl. Phys. Lett.* **97** 24–27
[37] Fu H and Cohen R E 2000 *Nature* **403** 281–3
[38] Von Helden L, Bogula L, Janolin P E, Hanke M, Breuer T, Schmidbauer M, Ganschow S and Schwarzkopf J 2019 *Appl. Phys. Lett.* **114** 232905